Acta Crystallographica Section D
Biological Crystallography
ISSN 1399-0047

Structure of the full-length yeast Arp7–Arp9 heterodimer

Joel Lobsiger, Yvonne Hunziker and Timothy J. Richmond*

Institute of Molecular Biology and Biophysics, Department of Biology, ETH Zürich, Schafmattstrasse 20, ETH-Hönggerberg, CH-8093 Zürich, Switzerland

Correspondence e-mail: richmond@mol.biol.ethz.ch

Received 17 July 2013
Accepted 6 October 2013

PDB reference: Arp7–Arp9 complex, 3wee

The nuclear actin-related proteins Arp7 and Arp9 are components of the yeast SWI/SNF and RSC chromatin-remodelling complexes. The 3.1 Å resolution crystal structure reported here shows that the full-length Arp7 and Arp9 proteins exist as a dimer without a requirement for additional polypeptides. Of the 11 actin-related proteins, Arp7 and Arp9 are the only two directly demonstrated to form a dimer within this family. The Arp7–Arp9 heterodimer is unlikely to form an actin-like filament based on modelling using the structure. The Arp7–Arp9 structure reveals that its dimerization interface is not altered when bound in a complex with the SWI/SNF Snf2 HSA domain and the regulatory protein Rtt102.

1. Introduction

The actin-related proteins Arp1–Arp11 and actin comprise the actin protein family, with genes for most members found in multiple eukaryotic species (Muller *et al.*, 2005). Arps are located both in the cytoplasm and the nucleus, where they are associated with the actin cytoskeleton and the microtubule-associated dynactin (Arp1, Arp2, Arp3, Arp10 and Arp11) and with a variety of chromatin-remodelling factors and heterochromatin complexes (Arp4, Arp5, Arp6, Arp7, Arp8 and Arp9, as well as actin), respectively (Schafer & Schroer, 1999; Machesky & May, 2001). These latter Arps and actin participate as subunits of one or more of the complexes SWI/SNF, RSC, INO80, SWR1 and NuA4 in *Saccharomyces cerevisiae*, BAP in *Drosophila melanogaster* and BAF, PBAF, p400 and Tip60 in mammals (Olave *et al.*, 2002; Szerlong *et al.*, 2008). The structures of Arp2 and Arp3 were found as non-interacting entities in the X-ray structure of the larger Arp2–Arp3 complex and were proposed to make contact during the process of actin-filament assembly (Robinson *et al.*, 2001). The ATP-bound crystal structures of yeast Arp4, yeast Arp8 and the actin-homology domain of human Arp8 have been determined (Fenn *et al.*, 2011; Gerhold *et al.*, 2012; Saravanan *et al.*, 2012). From solution studies, all three proteins were found to be monomeric, although full-length Arp8 was additionally observed to have a dimeric form. Co-expression of independently tagged Arp7 and Arp9 in *Escherichia coli* revealed that Arp7 and Arp9 behave as a heterodimer in pull-down assays (Szerlong *et al.*, 2003). The recent X-ray structure of a relatively small subcomplex from the 1 MDa yeast SWI/SNF bound to two additional polypeptides shows that Arp7 and Arp9 are interaction partners (Schubert *et al.*, 2013). In this structural context, the HSA domain of the SWI/SNF Snf2 subunit and a fragment of the Rtt102 regulatory protein both bridge between Arp7 and Arp9. The inclusion of the HSA and Rtt102 polypeptides, as well as the deletion of a segment of Arp9 to promote crystallization, may affect the interaction of

Arp7 and Arp9 in this Arp7–Arp9–HSA–Rtt102 complex. The structure of the Arp7–Arp9 heterodimer is important in its own right and in comparison to the version in Arp7–Arp9–HSA–Rtt102. Here, we report the structure of the isolated Arp7–Arp9 heterodimer using the full-length proteins of 477 and 467 amino acids, respectively.

2. Materials and methods

2.1. Gene cloning, protein expression and purification

The protein-expression plasmid containing the *S. cerevisiae Arp7* and *Arp9* genes was a gift from B. Cairns (Szerlong *et al.*, 2003). The Arp7 protein was fused at its C-terminus to a His-tag (PHHHHHHH). The Arp9 protein was fused by the replacement of its N-terminal methionine by a FLAG-tag (MDYKDDDDKG). The constructs were transformed into BL21 CodonPlus competent *E. coli* cells (RIPL, Stratagene), induced with isopropyl β-D-1-thiogalactopyranoside (IPTG) for expression, grown to an OD_{600} of 0.4 at 22°C and harvested by centrifugation. Cell pellets were flash-cooled in liquid N_2 and stored at −80°C. Cells were lysed by three passes through a French press (Thermo Electron Corporation) in 200 m*M* KCl, 25 m*M* Tris–HCl pH 8.0, 1 m*M* β-mercaptoethanol, 0.7 µg ml^{-1} pepstatin, 1.0 µg ml^{-1} leupeptin. The cell lysate was clarified by centrifugation twice at 15 000*g* for 45 min. The Arp7–Arp9 complex was purified using His-tag affinity and gel-permeation chromatography. The sample was washed on and eluted from TALON resin (BD Bioscience) with lysis solution containing 20 and 200 m*M* imidazole, respectively. The Superdex S200 column (GE Healthcare) was run in 200 m*M* KCl, 20 m*M* Tris–HCl pH 8.0, 0.5 m*M* ethylenediaminetetraacetic acid (EDTA). For crystallization, the purified fusion-protein complex was concentrated to 8 mg ml^{-1} in 200 m*M* KCl, 0.5 m*M* EDTA, 20 m*M* Tris–HCl pH 8.0 using a centrifugal filter concentrator (Amicon Ultra 10K).

2.2. Crystallization, X-ray data collection and structure determination

Arp7–Arp9 was crystallized at 4°C using sitting-drop vapour diffusion by mixing 2 µl protein stock with 2 µl reservoir solution (2 *M* sodium/potassium phosphate, 100 m*M* CAPS–NaOH pH 10.5, 200 m*M* lithium sulfate) and equilibrating against 60 µl reservoir solution. Methymercury derivatization was performed by soaking crystals for 2 h in reservoir solution brought to 5 m*M* in methymercury nitrate before back-soaking for 2 h in reservoir solution. Prior to X-ray exposure, crystals were successively soaked for 30 s in reservoir solution supplemented with 10, 15 and 20% glycerol and were then flash-cooled by immersion into liquid N_2.

X-ray diffraction data were measured at the Swiss Light Source, Villigen, Switzerland either on beamline PXI-X06SA (Pilatus 6M detector) for data sets from native and methylmercury-derivatized crystals or on beamline PXIII-X06DA (Pilatus 2M detector) for a data set optimized for sulfur anomalous signal (Kraft *et al.*, 2009; Doutch *et al.*, 2012). Data sets were processed with *XDS*, *SCALA* and *TRUNCATE* to yield scaled structure-factor amplitudes (Evans, 2006; Kabsch, 2010; Winn *et al.*, 2011).

Table 1
Crystallographic statistics.

Values in parentheses are for the highest resolution shell.

Data set	Native	CH_3HgNO_3-SAD	S-SAD
Space group	$P3_121$		
Unit-cell parameters (Å)	$a = b = 103.2$, $c = 185.3$	$a = b = 103.8$, $c = 184.5$	$a = b = 103.6$, $c = 185.7$
Wavelength (Å)	1.00604	1.00608	2.066
Resolution (Å)	29.6–3.20 (3.37–3.20)	29.7–3.10 (3.27–3.10)	30.0–3.60 (3.79–3.60)
Completeness (%)	99.3 (98.7)	99.9 (99.8)	99.9 (99.4)
Multiplicity	7.6 (7.7)	9.0 (9.1)	75.5 (75.5)
$\langle I/\sigma(I)\rangle$	20.2 (5.1)	18.1 (4.4)	34.1 (14.0)
$R_{\rm merge}$† (%)	9.4 (42)	10.3 (49)	15.0 (45)
Sites		7	27
Phasing power‡ (ano)		1.18	
Figure of merit§ (acentric/centric)		0.39/0.15	
Unique reflections		21472	
$R_{\rm cryst}/R_{\rm free}$¶ (%)		19.9 (29.3)/ 22.0 (34.2)	
No. of protein/water atoms		6763/0	
R.m.s.d., bond lengths (Å)		0.007	
R.m.s.d., bond angles (°)		1.11	
Mean *B* factor (Å^2)		70.3	
Ramachandran plot, residues in (%)			
Most favoured regions		96.1	
Additionally allowed regions		3.9	
Generously allowed regions		0.0	

† $R_{\rm merge} = \sum_{hkl}\sum_i |I_i(hkl) - \langle I(hkl)\rangle| / \sum_{hkl}\sum_i I_i(hkl)$, where $I_i(hkl)$ is the intensity of a structure factor and $\langle I(hkl)\rangle$ is the mean intensity of all symmetry-related structure factors. ‡ Phasing power = $\langle |F_{\rm H}(hkl)|/L(hkl)\rangle$, where $F_{\rm H}(hkl)$ is the calculated heavy-atom contribution for a structure factor and $L(hkl)$ is the phase-integrated lack of closure between observed and calculated derivative structure factors. § Figure of merit = $\langle \cos\Delta\alpha_i(hkl)\rangle$, where $\Delta\alpha_i$ is the phase-angle deviation for a structure factor. ¶ $R_{\rm cryst} = \sum_{hkl} ||F_{\rm obs}| - |F_{\rm calc}|| / \sum_{hkl} |F_{\rm obs}|$, where $|F_{\rm obs}|$ and $|F_{\rm calc}|$ denote the observed and calculated structure factor-amplitudes for 95% of the *hkl*. The remaining *hkl* are not used in refinement but are used to calculate $R_{\rm free}$ as for $R_{\rm cryst}$.

The crystal structure was solved to 3.1 Å resolution using the single-wavelength anomalous dispersion (SAD) method based on the methylmercury-derivative data set (CH_3HgNO_3-SAD; Table 1). Neither molecular replacement based on various actin structures using the native data set (native; Table 1) nor use of the sulfur anomalous-dispersion data set (S-SAD; Table 1) was successful. The methylmercury sites were found using *HySS* in the *PHENIX* suite (McCoy *et al.*, 2007; Adams *et al.*, 2010). Cross-validation of heavy-atom locations was performed using *SHELX* (Sheldrick, 2008). The phases and initial electron-density map were calculated with *Phaser* and *RESOLVE* (in *PHENIX*) and were cross-validated with *CNS* and *autoSHARP* (Adams *et al.*, 2010; Brünger *et al.*, 1998; McCoy *et al.*, 2007; Terwilliger, 2000). The electron-density map was initially fitted with two polyalanine chains corresponding to the yeast actin fold (PDB entry 1yag; Vorobiev *et al.*, 2003). The chain trace was modified based on fragments built automatically using *RESOLVE*, *Buccaneer* and *ARP/wARP* (Cowtan, 2006; Langer *et al.*, 2008). The model was improved by rigid-body refinement followed by simulated annealing with torsion-angle dynamics (initial temperature 3000 K, cooling rate 25 K, MLHL target) using

PHENIX and manual model building using *Coot* (Emsley *et al.*, 2010). An anomalous difference map calculated from the S-SAD data set aided the placement of cysteine and methionine residues, which then provided anchor points for further model building. Four sulfate ions and a molecule of *N*-cyclohexyl-3-aminopropanesulfonic acid (CAPS) could be located using the S-SAD map.

The model was iteratively optimized using *Coot* for model building and *PHENIX* for rigid-body, Cartesian coordinate, grouped *B*-factor, TLS displacement and anomalous scattering-factor refinement. The resulting model has acceptable $R_{\rm cryst}$ and $R_{\rm free}$ values and model geometry as determined using *PHENIX* (Table 1). Electron density was not observed for either the His-tag fused to Arp7 or the FLAG-tag fused to

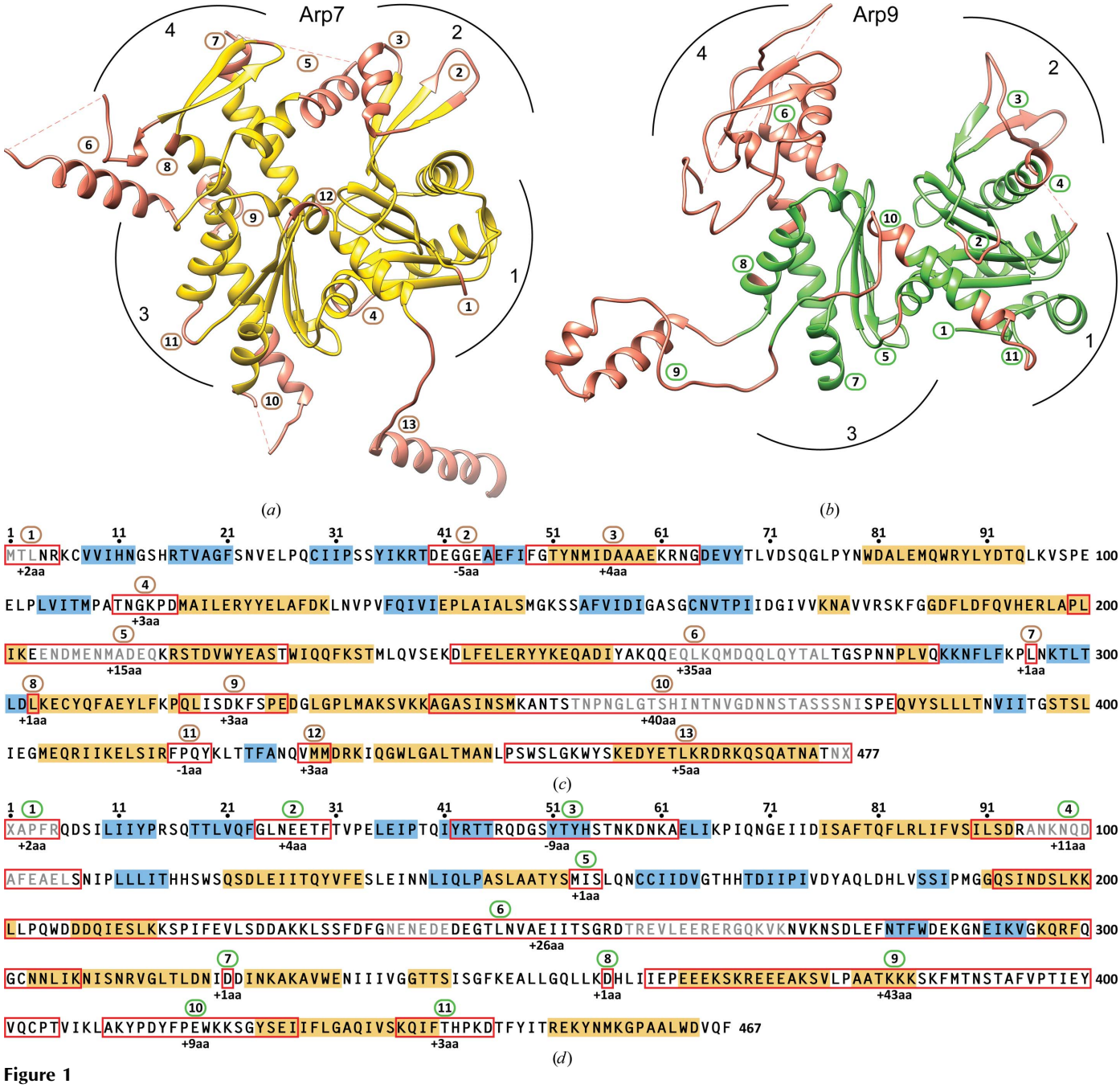

Figure 1
Structural comparison of Arp7 and Arp9 with actin. (*a*) The Arp7 monomer is shown with its regions of structural mismatch with *S. cerevisiae* actin highlighted (red) and consecutively numbered (circled). The subdomains 1–4 defined for actin are indicated. Connections (dotted lines) between two apparent termini owing to unobserved polypeptides are included for clarity. (*b*) The Arp9 monomer is shown as in (*a*). Arp7 and Arp9 were independently aligned with actin and are shown in the same orientation. (*c*) The Arp7 sequence is shown with the actin regions of mismatch (red rectangles) indicated with the same numbering as in (*a*). Secondary-structural elements (α-helices, gold; β-strands, blue) are highlighted. The number of amino acids inserted in Arp7 relative to actin are shown below the mismatched regions. Sequence segments not observed in the structure are indicated in grey. X represents a His-tag fused to the C-terminus of the native Arp7 protein of 477 amino acids. (*d*) The sequence of Arp9 is shown as in (*c*). X represents a FLAG-tag replacing the methionine at the N-terminus of the native Arp9 protein of 467 amino acids.

Arp9. Application of *Phaser* and *Coot* confirmed the accordance of the chain trace for the native data set. The Arp7–Arp9 atomic coordinates have been deposited in the Protein Data Bank (PDB entry 3wee).

3. Results and discussion

3.1. Structure of the Arp7–Arp9 heterodimer and comparison with actin

The full-length sequences of the *S. cerevisiae* Arp7 and Arp9 genes were co-expressed in *E. coli* and the protein products were isolated as a heterodimer and crystallized. The individual Arp7 and Arp9 structures were each independently aligned with the structure of *S. cerevisiae* actin determined in complex with gelsolin (Vorobiev *et al.*, 2003). The alignments were made with *Chimera* using main-chain C^{α} positions such that four consecutive positions not within 5 Å of each other were excluded (Yang *et al.*, 2012). Based on this criterion, the r.m.s. deviation is 1.70 Å between Arp7 and actin, with 86% of the C^{α} positions of the smaller actin paired. For Arp9, the r.m.s. deviation is 2.16 Å, with 78% of the C^{α} positions of the again smaller actin paired. The regions of structural mismatch (RM) with actin range from −9 to +43 amino acids in length and generally comprise insertions into actin loops connecting secondary-structural elements. They occur in all four of the canonical actin subdomains in both Arp7 and Arp9 (Fig. 1). The largest of these insertions, Arp9 RM9, with 43 additional amino acids, is well ordered and includes two α-helices. The other large insertions, Arp7 RM5, RM6 and RM10 and Arp9 RM4 and RM6, can include an additional α-helix but also encompass one or two stretches that are disordered in the Arp7–Arp9 X-ray structure. Deletions occur in Arp7 RM2 and Arp9 RM3 of subdomain 1, which in actin have a longer loop between antiparallel β-strands and an additional α-helix connecting the strands, respectively. Subdomain 4 of Arp9 is the most divergent over both structures based on the alignment of Arp7 and Arp9 using all four domains. When Arp9 subdomain 4 is aligned with actin on its own, the overall topology of the fold of the observed regions is similar, with 55% of the 115 amino acids aligning with an r.m.s. deviation of 2.09 Å. The two α-helices at the beginning and the two β-strands at the end of this subdomain are the main contributors to the match. Overall, the similarity in chain topology for Arp7, Arp9 and yeast actin is remarkable, as based on structural alignments Arp7 and Arp9 share only 21 and 15% sequence identity with yeast actin, respectively, and 7.5% with each other. The four previously defined hotspots (*A*–*D*) for differences between Arps and actin correspond to RM2 (*A*), RM7 (*B*), RM10 (*C*) and RM11 (*D*) in Arp7 and to RM2 (*A*), RM6 (*B*), RM7 (*C*), RM9 (*D*) and RM10 (*D*) in Arp9, accounting for 19 and 84% of the observed structurally mismatched amino acids, respectively (Muller *et al.*, 2005).

The structural alignments with actin show that the putative ATP-binding clefts of Arp7 and Arp9 in the heterodimer are accessible to solution, with the only potential steric hindrance to ATP binding being the G397S substitution in Arp7 relative to actin. This difference occurs in the conserved GG sequence

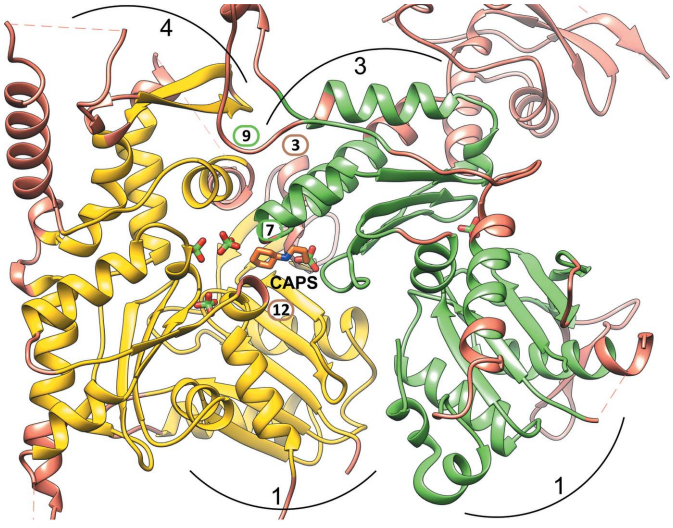

Figure 2
Arp7–Arp9 heterodimer. The Arp7–Arp9 heterodimeric unit is shown as observed in the crystal structure. The differences from actin, domains and regions are indicated as in Fig. 1. A molecule of CAPS from the crystallization solution is shown bound in a channel between the two subunits. The CAPS site is distinct from the cleft in each subunit that is homologous to the ATP-binding site in actin. The four sulfate ions shown are bound to these clefts in the heterodimer.

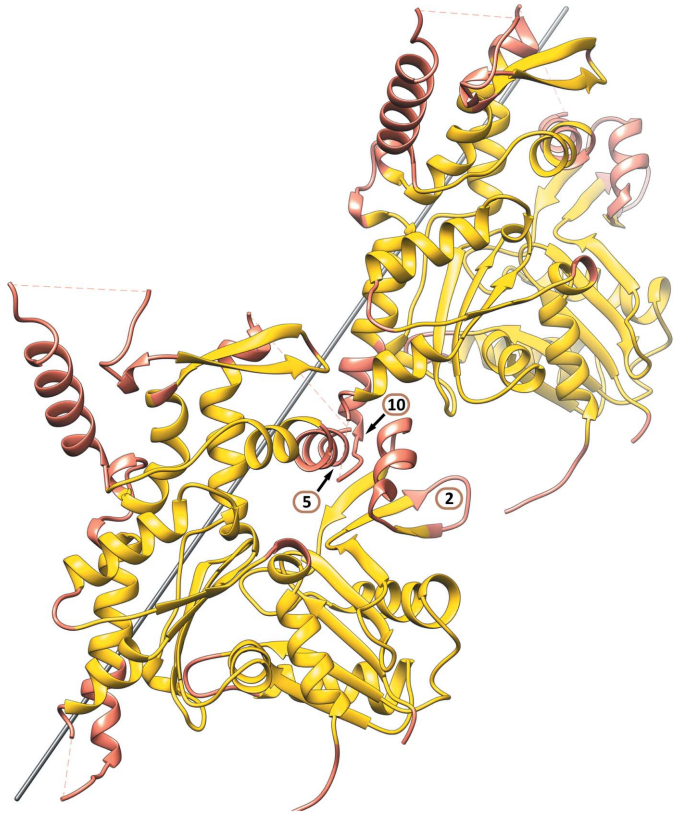

Figure 3
Barrier to an Arp7–Arp9 F-actin-like filament. Arp7 in one repeat along one strand of an F-actin-like filament is shown. The differences from actin are indicated as in Fig. 1. Arp9 is omitted for clarity of the intra-strand contacts. The filament axis is shown in grey.

(yeast actin, 301–302; Arp7, 396–397; Arp9, 337–338) noted with regard to ATP binding in the description of the original actin–DNase I structure (Kabsch *et al.*, 1990). The mutations S397Y in Arp7 and G338Y in Arp9 in the putative ATP-binding pockets were previously introduced *in vivo* and resulted in an unaltered yeast phenotype (Cairns *et al.*, 1998). Although a negative result, this lack of phenotypic change implies a lack of binding and hydrolysis of ATP by Arp7 and Arp9, and the current structural alignments show that the tyrosine side chain introduced in both cases would interfere with binding of the ribose moiety.

3.2. Dimerization interface and potential for filament formation

The heterodimeric interface between Arp7 and Arp9 consists primarily of interactions between Arp7 subdomain 1 spanning between Arp9 subdomains 1 and 3, including the

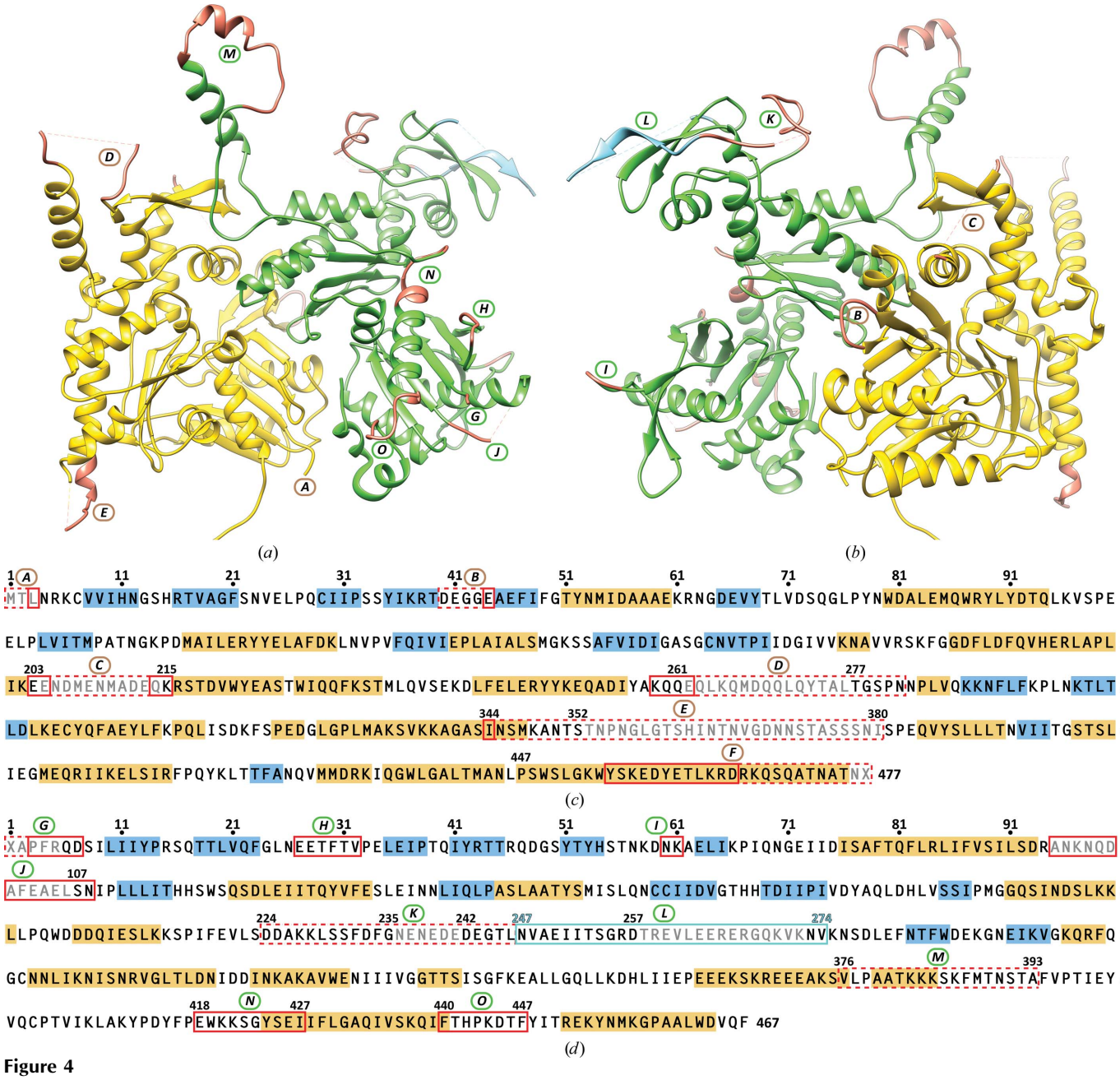

Figure 4
Structural comparison of Arp7–Arp9 with Arp7–Arp9–HSA–Rtt102. (*a*) The Arp7–Arp9 heterodimer with the regions of polypeptide chain that are a structural mismatch with the *S. cerevisiae* Arp7–Arp9–HSA–Rtt102 complex highlighted in red and consecutively lettered (circled). The region that was deleted from Arp9 in Arp7–Arp9–HSA–Rtt102 is indicated in cyan. The N-terminal α-helix of Arp7 corresponding to region *F* is not shown. (*b*) As in (*a*) but rotated 180° around a vertical axis. (*c*) The Arp7 sequence is shown with the regions of mismatch (red rectangles) with Arp7–Arp9–HSA–Rtt102. The labelling is the same as in (*a*) and (*b*). Secondary-structural elements (α-helices, gold; β-strands, blue) are highlighted. Sequence segments that are not observed in the Arp7–Arp9 structure are indicated in grey, as are unobserved regions in Arp7–Arp9–HSA–Rtt102 (red dotted rectangles). (*d*) The sequence of Arp9 is shown as in (*c*). The region that was deleted from Arp9 in Arp7–Arp9–HSA–Rtt102 is indicated (cyan rectangle).

regions Arp7 RM12 and Arp9 RM7, and between RM3 of Arp7 subdomain 2 and Arp9 subdomain 3 (Fig. 2). The channel formed in this interface clearly binds a molecule of CAPS (the pH buffer used for crystallization), as corroborated by the position of a sulfur anomalous scattering peak. Additionally, the chain at the N- and C-termini of Arp9 RM9 extends to make substantial contact with the β-strands of Arp7 subdomain 4 remote from the described interface. Overall, the dimerization interface comprises elements which are structurally homologous to actin, involving only four of the 23 RMs.

An Arp7–Arp9 filament model was made by superposition of the Arp7 subunit with each of the F-actin subunits of the 6.6 Å resolution F-actin protofilament structure (Fujii *et al.*, 2010). This construction places the Arp9 subunits on the outside of the two-stranded filament without creating any clashes, but provides potential stabilizing contacts between adjacent Arp9 subunits. Although the inter-strand contacts involve the overlap of Arp7 RM9 and RM10, the RM9 loop is likely to be sufficiently flexible to accommodate the close proximity. The axial contacts of Arp7, however, most probably block filament formation (Fig. 3). The main overlap occurs between the terminal extensions of α-helices in Arp7 RM10 (amino acids 345–352) and Arp7 RM5 (amino acids 215–219). Furthermore, the DNAse I-binding loop of actin, which makes an important axial contact in the actin protofilament, is reduced from ten to five amino acids in Arp7 RM2. The helix extension within Arp7 RM5 and the shorter DNAse I-binding loop were also noted as reasons for lack of filament formation for nuclear Arp4 (Fenn *et al.*, 2011). In contrast, the structure of nuclear Arp8 reveals an 83-amino-acid DNAse I-binding loop which loops around subdomain 4, blocking both the axial and inter-strand interactions observed in F-actin (Gerhold *et al.*, 2012). Rebuilding the filament model using superposition of Arp9 instead of Arp7 with actin results in extensively overlapped Arp7 subunits along the filament axis, thus ruling out Arp9 F-actin-like filaments.

3.3. Comparison of Arp7–Arp9 with Arp7–Arp9–HSA–Rtt102

Both the Arp7–Arp9 structure reported here and the structure of the Arp7–Arp9–HSA–Rtt102 complex (PDB entry 4i6m) reveal an Arp7–Arp9 heterodimer (Schubert *et al.*, 2013). No other polypeptides are present in the Arp7–Arp9 structure, but a CAPS molecule is bound in the dimerization interface. The Arp7–Arp9–HSA–Rtt102 complex contains the Snf2 HSA domain and a Rtt102 fragment in equimolar stoichiometry with an Arp7–Arp9 heterodimer. The region of HSA spanning Arp7 and Arp9 is 39 amino acids in length and is present as a single continuous α-helix. Three regions of the Rtt102 molecule are observed in the electron density (amino acids 1–12, 22–70 and 79–90), with the remainder presumably being too flexible to build into the map. The first and last of these regions contact only Arp7, while the middle region contacts both Arp7 and Arp9. Thus, both HSA and Rtt102 possibly stabilize or alter the interaction of Arp7 and Arp9 compared with the Arp7–Arp9 structure alone. Another potential factor affecting dimerization is the deletion of a stretch of 28 amino acids (247–274) from Arp9 subdomain 4 to facilitate crystallization of the Arp7–Arp9–HSA–Rtt102 complex. Nevertheless, superposition of the Arp7–Arp9 and Arp7–Arp9–HSA–Rtt102 structures, performed as for the structural comparisons of Arp7–Arp9 with actin, reveals only one difference in the heterodimer structure that is not plausibly explained by crystal contacts or by HAS and Rtt102 interactions (Fig. 4). The exception occurs for the Arp9 N-terminal amino acids 3–7, which have high temperature factors in both structures.

Although the solvent contents of 55 and 65% for Arp7–Arp9 and Arp7–Arp9–HSA–Rtt102, respectively, are not greatly dissimilar, the number of interacting neighbouring asymmetric units is significantly greater: ten for the Arp7–Arp9 crystals (space group $P3_221$) *versus* five for the Arp7–Arp9–HSA–Rtt102 crystals (space group $C2$). The dimer interface between Arp7 and Arp9 proposed in both structural studies is the only interface between structural elements that is common to both crystal forms. Again based on the criteria used for the alignments with actin, the r.m.s. deviation for the two Arp7–Arp9 structural units is 1.23 Å with 79% of the C^{α} positions paired. All 15 RMs (*A*–*O*) apparent from the alignment of the two Arp7–Arp9 structural units, with the exception of the Arp9 N-terminus (*G*), are accounted for by crystal-packing contacts or interactions with HSA (*N* and *O*) and Rtt102 (*F*, *J* and *N*). As a consequence of this analysis, we conclude that the structure of the Arp7–Arp9 heterodimer overall, as observed in two different crystal forms, is not affected either by binding of CAPS or by binding of HSA and Rtt102.

We thank D. F. Sargent for assistance with X-ray data collection at the Swiss Light Source (SLS), Paul Scherrer Institute.

References

Adams, P. D. *et al.* (2010). *Acta Cryst.* D**66**, 213–221.
Brünger, A. T., Adams, P. D., Clore, G. M., DeLano, W. L., Gros, P., Grosse-Kunstleve, R. W., Jiang, J.-S., Kuszewski, J., Nilges, M., Pannu, N. S., Read, R. J., Rice, L. M., Simonson, T. & Warren, G. L. (1998). *Acta Cryst.* D**54**, 905–921.
Cairns, B. R., Erdjument-Bromage, H., Tempst, P., Winston, F. & Kornberg, R. D. (1998). *Mol. Cell*, **2**, 639–651.
Cowtan, K. (2006). *Acta Cryst.* D**62**, 1002–1011.
Doutch, J., Hough, M. A., Hasnain, S. S. & Strange, R. W. (2012). *J. Synchrotron Rad.* **19**, 19–29.
Emsley, P., Lohkamp, B., Scott, W. G. & Cowtan, K. (2010). *Acta Cryst.* D**66**, 486–501.
Evans, P. (2006). *Acta Cryst.* D**62**, 72–82.
Fenn, S., Breitsprecher, D., Gerhold, C. B., Witte, G., Faix, J. & Hopfner, K. P. (2011). *EMBO J.* **30**, 2153–2166.
Fujii, T., Iwane, A. H., Yanagida, T. & Namba, K. (2010). *Nature (London)*, **467**, 724–728.
Gerhold, C. B., Winkler, D. D., Lakomek, K., Seifert, F. U., Fenn, S., Kessler, B., Witte, G., Luger, K. & Hopfner, K. P. (2012). *Nucleic Acids Res.* **40**, 11036–11046.
Kabsch, W. (2010). *Acta Cryst.* D**66**, 125–132.
Kabsch, W., Mannherz, H. G., Suck, D., Pai, E. F. & Holmes, K. C. (1990). *Nature (London)*, **347**, 37–44.

Kraft, P., Bergamaschi, A., Broennimann, Ch., Dinapoli, R., Eikenberry, E. F., Henrich, B., Johnson, I., Mozzanica, A., Schlepütz, C. M., Willmott, P. R. & Schmitt, B. (2009). *J. Synchrotron Rad.* **16**, 368–375.
Langer, G., Cohen, S. X., Lamzin, V. S. & Perrakis, A. (2008). *Nature Protoc.* **3**, 1171–1179.
Machesky, L. M. & May, R. C. (2001). *Results Probl. Cell Differ.* **32**, 213–229.
McCoy, A. J., Grosse-Kunstleve, R. W., Adams, P. D., Winn, M. D., Storoni, L. C. & Read, R. J. (2007). *J. Appl. Cryst.* **40**, 658–674.
Muller, J., Oma, Y., Vallar, L., Friederich, E., Poch, O. & Winsor, B. (2005). *Mol. Biol. Cell*, **16**, 5736–5748.
Olave, I. A., Reck-Peterson, S. L. & Crabtree, G. R. (2002). *Annu. Rev. Biochem.* **71**, 755–781.
Robinson, R. C., Turbedsky, K., Kaiser, D. A., Marchand, J. B., Higgs, H. N., Choe, S. & Pollard, T. D. (2001). *Science*, **294**, 1679–1684.
Saravanan, M., Wuerges, J., Bose, D., McCormack, E. A., Cook, N. J., Zhang, X. & Wigley, D. B. (2012). *Proc. Natl Acad. Sci. USA*, **109**, 20883–20888.
Schafer, D. A. & Schroer, T. A. (1999). *Annu. Rev. Cell Dev. Biol.* **15**, 341–363.
Schubert, H. L., Wittmeyer, J., Kasten, M. M., Hinata, K., Rawling, D. C., Héroux, A., Cairns, B. R. & Hill, C. P. (2013). *Proc. Natl Acad. Sci. USA*, **110**, 3345–3350.
Sheldrick, G. M. (2008). *Acta Cryst.* A**64**, 112–122.
Szerlong, H., Hinata, K., Viswanathan, R., Erdjument-Bromage, H., Tempst, P. & Cairns, B. R. (2008). *Nature Struct. Mol. Biol.* **15**, 469–476.
Szerlong, H., Saha, A. & Cairns, B. R. (2003). *EMBO J.* **22**, 3175–3187.
Terwilliger, T. C. (2000). *Acta Cryst.* D**56**, 965–972.
Vorobiev, S., Strokopytov, B., Drubin, D. G., Frieden, C., Ono, S., Condeelis, J., Rubenstein, P. A. & Almo, S. C. (2003). *Proc. Natl Acad. Sci. USA*, **100**, 5760–5765.
Winn, M. D. *et al.* (2011). *Acta Cryst.* D**67**, 235–242.
Yang, Z., Lasker, K., Schneidman-Duhovny, D., Webb, B., Huang, C. C., Pettersen, E. F., Goddard, T. D., Meng, E. C., Sali, A. & Ferrin, T. E. (2012). *J. Struct. Biol.* **179**, 269–278.